

# XTE J0111.2-7317 : a nebula-embedded X-ray binary in the SMC

M. J. Coe,<sup>1</sup> N.J. Haigh,<sup>1</sup> C.A. Wilson<sup>2</sup>, I. Negueruela<sup>3</sup>

<sup>1</sup>*Department of Physics and Astronomy, Southampton University, SO17 1BJ, UK*

<sup>2</sup>*NASA, MSFC, Huntsville, AL35812, USA*

<sup>3</sup>*Dpto. de Física, Ingeniería de Sistemas y Teoría de la Señal, Universidad de Alicante, Apdo. 99, E03080 Alicante, Spain*

Accepted . Received ; in original form

## ABSTRACT

The observed characteristics of the nebulosity surrounding the SMC High Mass X-ray Binary XTE J0111.2-7317 are examined in the context of three possible nebular types: SNR, bowshock and HII region. Observational evidence is presented which appears to support the interpretation that the nebulosity surrounding XTE J0111.2-7317 is an HII region. The source therefore appears to be a normal SMC Be X-ray binary (BeXRB) embedded in a locally enhanced ISM which it has photoionised to create an HII region. This is supported by observations of the X-ray outburst seen with BATSE and RXTE in 1998-1999. It exhibited characteristics typical of a giant or type II outburst in a BeXRB including large spin-up rates,  $Lx \geq 10^{38}$  erg/sq.cm-s, and a correlation between spin-up rate and pulsed flux. However, the temporal profile of the outburst was unusual, consisting of two similar intensity peaks, with the first peak of shorter duration than the second.

## 1 INTRODUCTION AND BACKGROUND

The X-ray transient XTE J0111.2-7317 was first detected by the Proportional Counter Array (PCA), on the Rossi X-ray Timing Explorer (RXTE) X-ray observatory, on October the 29th 1998 (Chakrabarty et al 1998a; Chakrabarty et al 1998b) in the 2-10keV band.

The observed temporal, flux and spectral characteristics are typical of BeXRBs and the detection of pulsations at 31 seconds further strengthens this hypothesis. In addition the source location is coincident with the SMC, the assumption of membership permitting an absolute luminosity to be calculated. Whilst towards the upper end of the typical flux distribution, peaking at approximately  $2 \times 10^{38}$  ergs<sup>-1</sup>, it is consistent with a giant (Type II) outburst from a BeXRB.

The optical counterpart was identified by Israel et al (1999) and subsequently optical and IR measurements by Coe, Haigh and Reig 2000 (henceforth referred to as CHR) confirmed the optical counterpart to be a B0-B2 luminosity class III-V star showing a strong IR excess. Surprisingly, however, their  $H\alpha$  images of the field revealed an extended region of  $H\alpha$  emission surrounding the source. They suggested it could be a surrounding SNR or wind bow shock. Otherwise XTE J0111.2-7317 is in many ways typical of the growing population of known SMC BeXRBs. If a SNR the size of 3.1pc, using the diameter-to-age relationship  $D = 0.9t^{2/5}$  (Clark & Caswell 1976), implies an age of 120yrs. A typical expansion velocity of 10000km/s (Chevalier 1977) for Type II SNe implies an age of  $\sim 300$ years. Such a young BeXRB would be of particular interest.

Throughout this work XTE J0111.2-7317 refers both to the X-ray source and to the optical counterpart.

## 2 OBSERVATIONS

### 2.1 Optical images

Initial photometry was reported by CHR who carried out Johnson, Strömgren and IR measurements. For this work further Wide Field Imager (WFI) images of the field taken on 26 July 1999 were extracted from the ESO archive. The WFI is a focal reducer-type camera which is permanently mounted at the Cassegrain focus of the 2.2-m MPG/ESO telescope at La Silla, Chile. The detector is a mosaic of  $4 \times 2 \times 4096 \times 8192$  CCDs with 0.24'' pixels. These observations targeted a different object, but because of the large  $34' \times 33'$  field XTE J0111.2-7317 was also imaged. Useful images in [SII],  $H\alpha$ , [OIII] and continuum regions close to  $H\alpha$  were de-archived. Preprocessing was performed using STARLINK software.

### 2.2 IR measurements

The source was observed as part of the DENIS IR survey of the Magellanic Clouds in Sept 1996. This IR catalogue shows  $I=15.27 \pm 0.02$  and  $J=15.19 \pm 0.10$  measurements, but not  $K_S$ , because of the source's faintness. However, a Service Observation of the field was carried out using IRIS2 on the AAT during commissioning time. The resulting K band image was calibrated using three DENIS sources in the field and

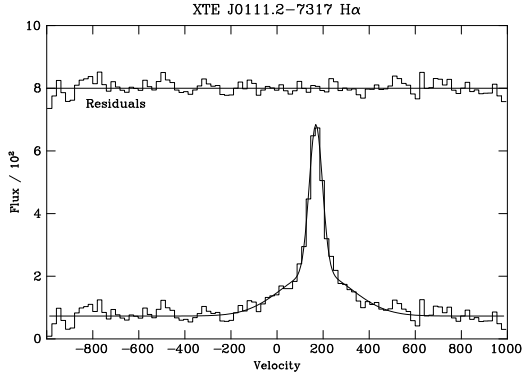


**Figure 1.**  $H\alpha$  region of SAAO XTE J0111.2-7317 spectrum with 2 component Gaussian fits.

an accurate determination of  $K=14.79\pm 0.03$  was achieved. The resulting J-K value of 0.4 is typical of other BeXRB systems in the SMC and indicative of an excess IR flux over the stellar continuum for the B0-B2 III-V star classified by CHR.

### 2.3 Optical spectroscopy

A blue spectrum was obtained at the ESO 1.52m telescope at La Silla, Chile, on November the 3rd 1999. The Boller and Chivens spectrograph was used with the no: 33 holographic grating, covering the range from the classification region (4000 – 5000Å) up to  $\sim 5900\text{\AA}$  with a resolution of 1Å per pixel. The slit was oriented in a NW-SE line to encompass the brightest parts of the nebulosity.

CHR reported results from spectroscopy in which the only features seen were strong  $H\alpha$  and  $H\beta$  emission lines, as expected for a BeXRB. The measured equivalent widths were  $-27\pm 0.3\text{\AA}$  for  $H\alpha$  and  $-3.8\pm 0.2\text{\AA}$  for  $H\beta$ . However, a considerable fraction of this emission is contamination from the nebular emission which crosses the stellar spectrum. Because the nebulosity is brightest close to the star, the sky/background subtraction carried out as a standard procedure in the spectral reduction does not remove such contamination. The nebular [SII] lines at 6716Å and 6731Å contaminate the stellar spectrum in the same way. All published equivalent widths to date (CHR and Covino et al. 2001) have been skewed by this effect.

Figure 1 shows the  $H\alpha$  region of the SAAO XTE J0111.2-7317 spectrum reported in CHR. Inspection of the spectral images shows that while the nebular contamination is fully contained in a band 5 pixels wide ( $\sim 2.1\text{\AA}$  or 97km/s), the true circumstellar emission is considerably broader at  $\sim 400\text{km/s}$ , typical for Be stars. Thus whilst the measured EW is certainly an overestimate, there is no doubt that intrinsic circumstellar emission exists. A two component Gaussian fit to the line profile was performed within the DIPSO/ELF package using the measured FWHM of the nebular contamination (obtained at a spatial position adjacent to the star) to robustly remove it (Figure 1). This fit assigns  $61\pm 4\%$  of the line flux to the broader circumstel-

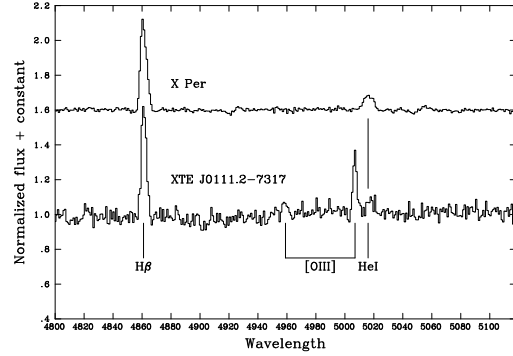


**Figure 2.** The 4800–5050Å region of the ESO spectrum of XTE J0111.2-7317 showing  $H\beta$ , [OIII] and HeI emission lines. The same range of a spectrum of the classic BeXRB X Per from the same observing run is shown for comparison. The XTE J0111.2-7317 spectrum has been shifted by  $-165\text{km/s}$  to the heliocentric rest frame.

lar disc (conventional Be) component, producing an intrinsic  $EW_{H\alpha}$  of  $16.5\pm 1.1\text{\AA}$ .

The Doppler shift of the broad circumstellar component of  $H\alpha$  is recessional at  $170.8\pm 9.3\text{km/s}$  (visible in Figure 1) which agrees well with the systemic value of  $166\pm 3\text{km/s}$  (Feast, 1961) for the SMC. Not only does this confirm membership of the SMC (never really in doubt because of the X-ray flux and photometry) but it also places a constraint on the system’s radial velocity relative to the local ISM of  $2.5\pm 12.5\text{km/s}$ . Accurate Doppler shifts for all of the lines detected from the surrounding nebulosity are in Table 2.

Regarding a classification based upon spectroscopic features, this has been done by Covino et al. (2001) based upon superior spectra, and their conclusion of B0.5-1Ve is consistent with this work.

Spectra (Figure 2) show lines at 4959Å and 5007Å, attributed to [OIII] emission. Such forbidden line emission is typical of many nebulae but uncharacteristic of the relatively dense circumstellar environment of Be stars. A search through the spectra of 11 other LMC/SMC BeXRB spectra in the Southampton database, and several galactic systems (including X Per and A0535+262) found no other systems with features at this wavelength (as expected if it arises from [OIII] emission). It is shown below that this feature results from the superposition of nebular emission.

### 2.4 X-ray data

#### 2.4.1 Observations

XTE J0111.2-7317 was active in X-rays from 1998 October - 1999 February. Figure 3 shows the 2-10 keV flux history measured with the All-Sky Monitor (ASM) (Levine et al, 1996) on the RXTE. XTE J0111.2-7317’s location was in the field-of-view of the RXTE PCA (Jahoda et al, 1996) and High Energy Timing Experiment (HEXTE) (Rothschild et al.1998) for 42 observations from 1998 October 20 - 1999 May 11. Further, the Burst and Transient Source Experiment (BATSE) (Fishman et al, 1989) on the Compton Gamma Ray Observatory had also observed XTE

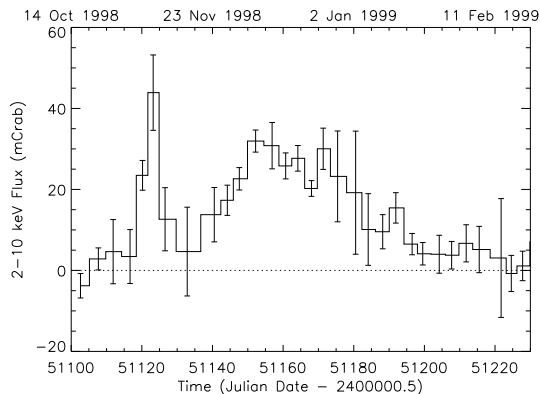


**Figure 3.** 2-10 keV flux history for XTE J0111.2–7317 measured with the RXTE ASM. All points are 4-day averages.

J0111.2–7317’s location from 1991-2000. No additional outbursts have been detected with either BATSE or RXTE.

#### 2.4.2 Timing

To determine pulse frequencies for XTE J0111.2–7317, we performed a grid search over a range of candidate frequencies using 1-second resolution 20-50 keV data from the BATSE Large Area Detectors (LADs). This technique is described in detail elsewhere (Finger et al, 1999; Wilson-Hodge 1999; Wilson et al, 2002; Wilson et al, 2003). First we combined the count rates over the 4 LADs viewing XTE J0111.2–7317, using weights optimized for an exponential energy spectrum  $f(E) = A \exp(-E/kT)$  with temperature  $kT = 12$  keV, and then grouped them into 300-s segments. In each 300-s segment, we fitted a model consisting of a sixth-order Fourier expansion in pulse phase model (representing the 20-50 keV pulse profile) and a spline function with quadratics in time (representing the background). Using 300-s segments allowed use of a quadratic background model, allowed us to effectively fit bright Earth occultation steps in the data, improved computational efficiency, and reduced smearing of the pulse profiles if the initial phase model was incorrect. The final step was to perform a grid search in frequency using the set of typically several hundred estimated 20-50 keV pulse profiles in each 4-day interval of data. For each grid point, the segment pulse profiles were shifted according to the corresponding frequency offset. These profiles were then combined into a mean profile. The best frequency was selected using a modified  $Z_n^2$  statistic, called  $Y_n$  after (Finger et al, 1999), given by  $Y_n = \sum_{h=1}^n |\bar{\alpha}_h|^2 / \sigma_{\bar{\alpha}_h}^2$ , where  $\bar{\alpha}_h$  is the mean Fourier coefficient for harmonic  $h$  and  $\sigma_{\bar{\alpha}_h}^2$  is the sample variance from the segment profiles. Using sample variances from the segment profiles rather than assuming Poisson statistics properly accounted for aperiodic noise in XTE J0111.2-7317 and in any other sources in the large BATSE field of view. A similar technique was used to generate pulse frequency measurements for RXTE PCA observations from 2-60 keV Standard 1 (125 ms, no energy resolution) data and from RXTE HEXTE data. The root-mean-squared (rms) pulsed fluxes were estimated at the best fit frequency as  $F_{\text{RMS}} = (0.5 \sum_{h=1}^m |\bar{\alpha}_h|^2)^{1/2}$ . Figure 4 shows the barycentered pulse frequency history measured

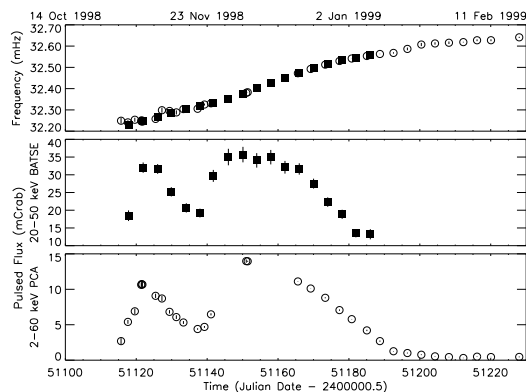


**Figure 4.** Top: Barycentered pulse frequencies measured with BATSE (filled squares) at 4-day intervals and measured with the RXTE PCA for each observation (open circles). Center: 20-50 keV pulsed flux measured with BATSE at 4-day intervals. (1 mCrab =  $1 \times 10^{-11}$  ergs  $\text{cm}^{-2}$   $\text{s}^{-1}$ ) Bottom: 2-60 keV pulsed flux measured with the RXTE PCA for each observation. (1 mCrab =  $2.786$  cts  $\text{s}^{-1}$   $\text{PCU}^{-1}$ )

with BATSE (squares) and with the RXTE PCA (open circles), the 20-50 keV pulsed flux measured with BATSE, and the 2-60 keV pulsed flux measured with the RXTE PCA. Pulsations were detected with BATSE from 1998 October 30 - 1999 January 9. The RXTE PCA continued to detect pulsations until observations ceased on 1999 February 19. Pulsations were not detected in two subsequent PCA observations on 1999 March 26 and 1999 May 11.

Pulse frequency derivatives were computed by differencing adjacent BATSE pulse frequency measurements. Figure 5 shows the correlation between frequency derivative and 20-50 keV pulsed flux. This correlation is well fitted with a power law with index  $0.9 \pm 0.1$ , which is consistent with the index of  $6/7$  expected from simple accretion theory, if accretion from a disk is assumed. If a reliable bolometric correction can be derived for a source, this correlation can be used to constrain the distance or the magnetic field strength if the other is known. Unfortunately in this case, large changes in the pulse fraction over the course of the outburst prevented us from deriving a reliable bolometric flux (see Figure 6).

#### 2.4.3 Energy Spectra

Analysis of the energy spectrum of XTE J0111.2–7317 was complicated by the fact that SMC X–1 was also present in the RXTE PCA and HEXTE field-of-view in many of our observations. Using power spectra from each observation, we determined in which observations 31-s pulsations from XTE J0111.2–7317 were present and 0.7-s pulsations from SMC X–1 were not present. We then generated energy spectra and response matrices for the PCA and HEXTE data for these 20 observations and fitted them in XSPEC with an absorbed power-law with a high energy cut-off and a Gaussian iron line. Average parameter values for the 20 observations are given in Table 1. The flux in the iron line was correlated with the total flux, with a correlation coefficient of 0.97 and a chance probability of  $2.5 \times 10^{-5}$ , suggesting that the iron line is intrinsic to XTE J0111.2–7317. No other parameters

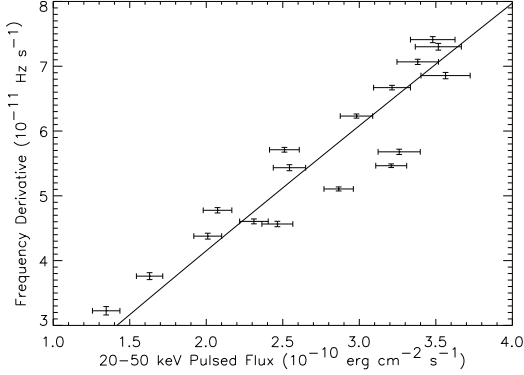


**Figure 5.** Frequency derivatives versus 20-50 keV pulsed flux measured with BATSE. The solid line denotes a power law fitted to these data with an index of  $0.9 \pm 0.1$ .

were obviously correlated with flux nor did they show clear evolution with time.

Using only those observations where SMC X-1 was not present in the power spectrum, we estimated pulse fractions from RXTE PCA data. Figure 6 shows the pulse fraction versus the 2-50 keV flux computed from our XSPEC fits. The pulse fraction is correlated with the total flux, indicating that the increase in flux is primarily in the pulsed component.

### 3 DISCUSSION

#### 3.1 The X-ray observations

Comparing BATSE and PCA pulsed fluxes, we see evidence that the first peak of the outburst is harder than the second peak, shown in Figure 7. Unfortunately, because SMC X-1 is present in all of the observations during the first peak of the outburst, we cannot study the effects of this change in hardness on the shape of the energy spectrum in detail. The physical explanation of this is unclear. We speculate that this may be an obscuration or absorption effect - the softer X-rays are partially absorbed or blocked by the large amount of material present at the beginning of the outburst. As the outburst progresses, this material begins to dissipate and the softer X-rays become more easily seen. A comparison of HEXTE and PCA pulsed fluxes suggests a similar change in hardness, although the HEXTE fluxes are much less certain than the BATSE fluxes due to the smaller effective area and integration time. This suggests that the effect is intrinsic to the source and is most likely not instrumental.

Observations of steady spin-up during the outburst allow us to compute a lower limit to the luminosity of XTE J0111.2-7317. The angular momentum of a rotating neutron star is given by  $\ell = 2\pi I\nu$  where  $\nu$  is the spin frequency and  $I$  is the moment of inertia of the neutron star. The torque on the neutron star is obtained by differentiating  $\ell$  or  $N = \dot{\ell} = 2\pi I\dot{\nu}$ . In an accreting pulsar undergoing steady spin-up, the characteristic torque is given by  $N_{\max} = \dot{M}(GM_X r_m)^{1/2}$  where  $\dot{M}$  is the mass accretion rate,  $G$  is the gravitational constant,  $M_X$  is the mass of the neutron star, and  $r_m$  is the magnetospheric radius. The max-

**Table 1.** X-ray Spectral Parameters for XTE J0111.2-7317

| Parameter                           | Value                | Standard Deviation   |
|-------------------------------------|----------------------|----------------------|
| $N_{\text{H}}$ ( $\text{cm}^{-2}$ ) | $1.5 \times 10^{22}$ | $0.5 \times 10^{22}$ |
| index                               | 0.93                 | 0.06                 |
| $E_{\text{cut}}$ (keV)              | 13.4                 | 0.8                  |
| $E_{\text{fold}}$ (keV)             | 20.3                 | 2.2                  |
| $E_{\text{line}}$ (keV)             | 6.5                  | 0.2                  |
| $\sigma_{\text{line}}$ (keV)        | 0.8                  | 0.5                  |

imum possible torque occurs when the magnetospheric radius equals the corotation radius. Setting  $N \leq N_{\max}$  yields an expression for  $\dot{M}$  and hence  $L_X$  that depends only on the spin frequency and its derivative for assumed values of the neutron star parameters, i.e.

$$L_X \geq (2\pi)^{4/3} I (GM_X)^{1/3} R_X^{-1} \dot{\nu} \nu^{1/3}. \quad (1)$$

Assuming  $I = 10^{45} \text{ g cm}^2$ ,  $M_X = 1.4M_{\odot}$ , and  $R_X = 10 \text{ km}$ ,  $L_X \geq 10^{38} \text{ ergs s}^{-1}$  for typical observed values of  $\nu = 32.4 \text{ mHz}$  and  $\dot{\nu} = 5 \times 10^{-11} \text{ Hz s}^{-1}$ . The average 20-50 keV pulsed flux was  $2.5 \times 10^{-10} \text{ ergs cm}^{-2} \text{ s}^{-1}$ , implying that XTE J0111.2-7317 is at a distance of  $d \geq 59.8 \text{ kpc}$ , confirming that it is in the SMC.

The outburst from XTE J0111.2-7317 should be classified as a giant or Type II outburst given the large spin-up rates  $(3-7) \times 10^{-11} \text{ Hz s}^{-1}$  measured with BATSE and the large luminosities  $(2-9) \times 10^{38} \text{ ergs s}^{-1}$ , measured in the PCA observations where SMC X-1 was not present. However, the temporal profile of this outburst is unlike giant outbursts in other Be/X-ray binaries that typically consist of either a single large intensity peak or a large peak followed by smaller peaks modulated at the orbital period. The initial large peak is usually much brighter and of much longer duration than any succeeding peaks. XTE J0111.2-7317 instead has two peaks that are similar in intensity with the first peak lasting about 25 days and the second lasting about 60 days, followed by a declining tail lasting about 30 days. The separation between the two peaks is about 30 days. This double peaked structure is most likely not due to orbital effects because the frequency derivative is strongly correlated with the pulsed flux and also shows the double peaked structure. Such a correlation is predicted by simple accretion theory for systems accreting from a disk. If the primary source of spin-up was orbital, we would not expect a strong correlation with the pulsed flux and we would expect to see both increases and decreases in pulse frequency as the pulsar moved relative to the observer.

#### 3.2 The nebulosity

The low surface brightness of the nebulosity, and the presence of faint field stars superimposed upon it and nearby, combine to make a morphological interpretation difficult. The  $H\alpha$  image of XTE J0111.2-7317 taken from the ESO data shows the nebulosity clearly but it is unclear whether some of the brighter patches are stars or enhanced nebular emission. However, because the  $H\alpha$  filter bandpass is effectively a subset of the broader R filter, the stellar continuum emission present in the  $H\alpha$  images can be largely removed using an R band image.

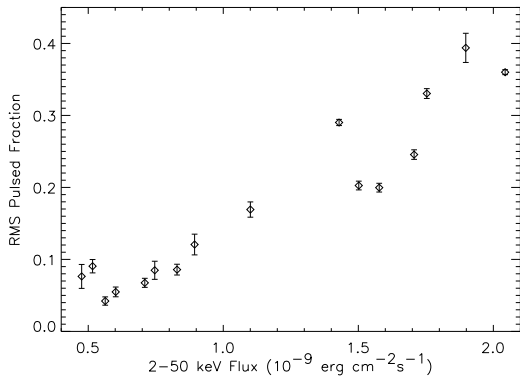


**Figure 6.** Root mean squared pulse fraction versus 2-50 keV flux for XTE J0111.2-7317.

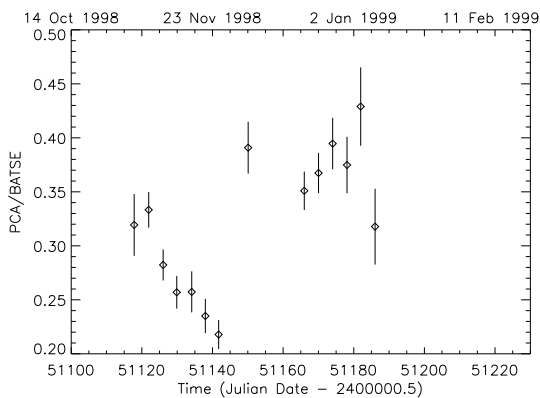


**Figure 7.** Ratio of the 2-60 keV pulsed flux in mCrab units measured with the RXTE PCA to the 20-50 keV pulsed flux in mCrab units measured with BATSE.

The final result shows that the emission is smoother than would appear from the  $H\alpha$  image alone, though two slightly brighter features are weakly visible to the SSW.

### 3.2.1 Image characteristics

Initial analyses of the nebula used CCD imaging from the SAAO 1.0m provided the ‘first look’. Though images were obtained in all filters, only the  $H\alpha$  image shows nebulosity. Though  $H\beta$  emission is present (Table 2), it is apparently too weak to register in the image, due both to the large amount of continuum also transmitted and to the poor response of the CCD in the blue.

However these data were to some extent superseded by the archival images from the ESO 2.2m telescope due to their superior depth and resolution. Images in  $H\alpha$ ,  $H\alpha$  continuum, [OIII] and [SII] were dearchived, but again only  $H\alpha$  clearly displayed nebulosity (Figure 8). Continua were removed for both the [SII] and [OIII] images. Unfortunately only  $H\alpha$  continuum images were available to model the continuum component; this was not a problem with [SII] (at  $\lambda 6717, 6731$  c.f.  $H\alpha$  at  $\lambda 6563$ ) because of the minimal spectral separation, but the [OIII]  $\lambda 5007$  continuum was not adequately represented by the  $H\alpha$  continuum image, thus leaving significant stellar images and preventing the detection

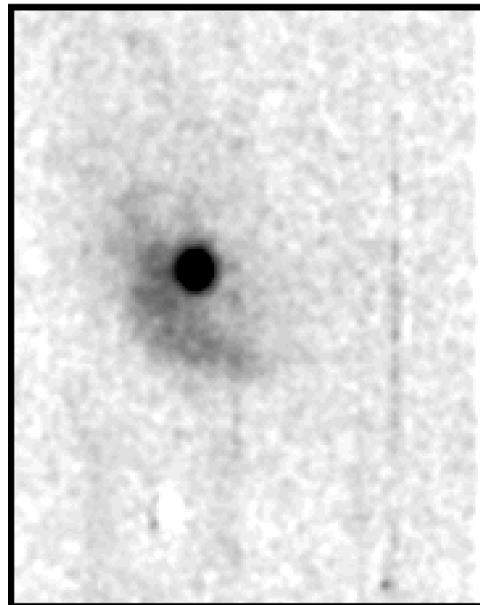


**Figure 8.** Continuum subtracted  $H\alpha$  image of the region around XTE J0111.2-7317. Image from ESO La Silla 2.2m archive, smoothed with a  $\sigma = 1''$  Gaussian filter. Bright and dark lines are due to bad CCD columns. Image size is  $\sim 40 \times 50$  arcsec.

of the small [OIII] nebula (Section 3.3.4). The FWHM of XTE J0111.2-7317 was measured both in the un-subtracted and continuum-subtracted [OIII] images and found to be consistent with the other field stars. [SII] appears to show extremely weak emission coincident with  $H\alpha$ .

Thus analyses of the structure of the nebula in the light of these species were undertaken spectroscopically (see below). Using the maximum diameter  $D$  of  $20''$  at a distance of 63.1pc one arrives at a diameter of 6.1pc for the  $H\alpha$  nebulosity.

Of the possible nebular types considered the simplest is a conventional HII region, photoionised by XTE J0111.2-7317. A second possibility is that the nebula is an SNR. In view of the association with the BeXRB system, it would be extremely interesting to identify the SNR corresponding to the formation of the system’s neutron star. This would, amongst other things, enable the system’s age to be determined.

Another possibility which exists is that the nebulosity is a bowshock. Such structures arise when ram pressure due to supersonic motion of a star confines its expanding wind. The head or apex of the structure defines a point where the momentum of the expanding stellar wind balances that of the oncoming interstellar medium. Bowshocks are commonplace around OB runaway stars. Indeed, according to the standard theory of BeXRB formation, such systems MUST be runaways (van den Heuvel et al, 2000). Therefore bowshocks could be commonplace around BeXRBs. The nature of the nebula is discussed below.

### 3.2.2 Nebular spectrum extraction

No nebulosity had been observed when the SAAO spectra were taken so the exposures were calculated to properly expose for the Be star. However since the slit of the spec-

trograph was aligned E-W subsequent examination of the raw spectral images revealed weak nebular emission lines offset to one side of the stellar continuum. This one-sidedness stems from the asymmetrical morphology of the nebulosity.

Two spectra of the source were acquired, the second because the intended star largely missed the slit on the first. However both contained strong nebular features, and so were co-added. The exposures were sequential and as a pair were bracketed by arc exposures; no wavelength shift was detectable. All further reduction took place on this co-added image.

The SAAO blue exposure similarly shows only very weak nebular  $H\beta$  emission. In view of the existence of a far higher S/N blue spectrum from La Silla, no further work was undertaken on the blue SAAO spectrum.

Thus the STARLINK task EXTRACT was used to extract the region immediately adjacent to the star including these emission features; sky subtraction was from a region 10 pixels below. Whilst sky subtraction was used to identify and reject telluric and other non-nebular lines, actual measurement used subtraction of a constant background to significantly reduce noise. This also enabled telluric lines to be used as wavelength standards, for example the  $3.682\text{\AA}$  separation of telluric  $H\alpha$  from its SMC component provides a highly accurate velocity. Care was taken to exclude any stellar (including Be circumstellar disc) flux. Table 2 lists the nebular emission lines obtained from the SAAO red and ESO blue spectra.

The ESO blue spectra taken on 3 November 1999 were extracted using the same method.

Dividing the  $H\alpha$  flux density integrated along the slit by the approximate scale of  $8''$  for the object one derives a  $H\alpha$  flux density of  $\sim 20 \times 10^{-16} \text{ erg/cm}^2/\text{s/arcsec}^2$ , which is close to the value found for the bowshock associated with Vela X-1 (Kaper et al, 1997) of  $\sim 10 \times 10^{-16} \text{ erg/cm}^2/\text{s/arcsec}^2$ .

Because of the small number of counts from the nebular lines, the extracted spectra are a spatial average over all the nebulosity which fell upon the spectrograph slit. Without higher S/N data this is the only way of extracting spectra of usable quality. Discussion on the spatial distribution of the different emission lines is presented below.

### 3.2.3 Line fitting

In order to derive the most accurate line fluxes the Emission Line Fitting (ELF) suite within DIPSO was employed. The FWHM values were specified from measurement of the  $H\beta$  line to reduce the number of free parameters and thus errors. The final fit is shown in Figure 9.

The velocities are derived from the shift relative to laboratory rest wavelengths, and further corrected to a heliocentric reference frame using the STARLINK program RV. The positive values refer to a movement away from the observer, i.e. a redshift.

### 3.2.4 Line flux calibration

The presence of the stellar continuum alongside the nebular spectrum allows an absolute flux calibration to be performed. Such calibration is important for establishing reliable line ratios for diagnostic techniques.

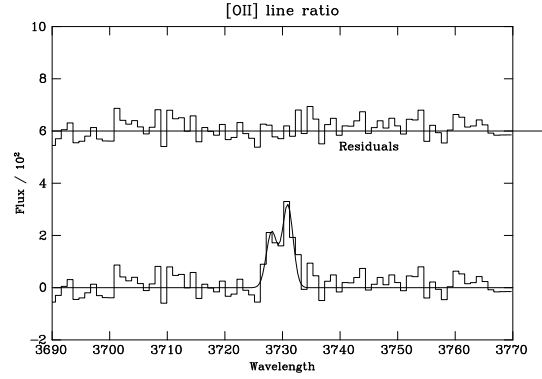


**Figure 9.** Gaussian fit to the [OII]  $\lambda 3727, 3729$  lines seen in the nebulosity around XTE J0111.2-7317.

The reddened theoretical Kurucz model photospheric spectrum (Kurucz, 1979) fitted by CHR was further reddened to allow for the circumstellar reddening. This was normalized using the photometry at B and R for the blue and red spectra respectively. The extracted stellar spectrum was divided into this and fitted with a polynomial yielding the required scaling factor at each wavelength to convert from counts (the units of the line fitting) to  $\text{erg/cm}^2/\text{s/\AA}$ . Clearly this calibration technique is dependent upon the Kurucz atmosphere being an accurate model of the true stellar spectrum. Note however that only the shape of the spectrum within each spectral range is important; the normalization, which is performed using photometry approximately in the centre of each range, ensures that the flux density is correct at this point and thus near the mark over the entire spectral range.

## 3.3 Spectral results

### 3.3.1 Temperature.

The O line strengths constrain the nebular electron temperature to below 25-40,000K; in fact standard nebular theory provides a mechanism to maintain the temperature in the range 5000 - 10000K. Collisions of high energy electrons with ionised O, Ne, S and Fe excite these ions into the metastable states which subsequently decay by photon emission. This mechanism can be seen to be at work from the high intensity of O and S forbidden lines. This effectively limits the electron temperature to 10000K with a mean value of 6700K (Kitchen 1987). The consistency with which this mechanism has been seen to provide a 'thermostat' controlling the temperature of nebulae provides encouragement that it also applies in this case.

### 3.3.2 Nebular Density.

[OII] and [SII] both emit close pairs of optical lines whose ratios are diagnostic of  $N_e$ , the electron density (Saraph & Seaton, 1970). Using ratios of lines produced by the same species is appealing as uncertainties based on abundance, degree of ionization and the many other variables cancel out. This diagnostic tool is based upon the increasing effect of collisional de-excitation in preventing the emission of a pho-

| Species                            | $\lambda$<br>( $\text{\AA}$ ) | Rest $\lambda$<br>( $\text{\AA}$ ) | Flux per arcsec<br>( $10^{-16} \text{ erg/cm}^2/\text{s}$ ) | Velocity<br>(km/s) | FWHM<br>(km/s) |
|------------------------------------|-------------------------------|------------------------------------|---|--------------------|----------------|
| ESO blue<br>3600–5900 $\text{\AA}$ |                               |                                    |   |                    |                |
| [OII]                              | $3728.12 \pm 0.14$            | 3726.16                            | $25.3 \pm 3.7$  | $145.3 \pm 10.8$   | $176 \pm 20$   |
| [OII]                              | $3730.91 \pm 0.14$            | 3728.91                            | $37.4 \pm 4.0$  | $148.4 \pm 10.8$   | $176 \pm 20$   |
| H $\gamma$                         | $4343.10 \pm 0.43$            | 4340.47                            | $10.0 \pm 2.7$  | $169.7 \pm 29.4$   | $217 \pm 60$   |
| H $\beta$                          | $4864.31 \pm 0.10$            | 4861.33                            | $17.7 \pm 1.3$  | $172.0 \pm 6.0$    | $189 \pm 19$   |
| [OIII]                             | $4961.89 \pm 0.23$            | 4958.91                            | $2.8 \pm 1.2$   | $168.1 \pm 13.6$   | $171 \pm 39$   |
| [OIII]                             | $5009.82 \pm 0.23$            | 5006.84                            | $7.7 \pm 1.4$   | $166.4 \pm 13.5$   | $170 \pm 39$   |
| SAAO red<br>6180–6930 $\text{\AA}$ |                               |                                    |   |                    |                |
| H $\alpha$                         | $6566.28 \pm 0.02$            | 6562.76                            | $150.5 \pm 3.5$   | $168.3 \pm 8.3$    | $66 \pm 2$     |
| [SII]                              | $6720.03 \pm 0.06$            | 6716.47                            | $25.1 \pm 3.5$  | $163.7 \pm 5.7$    | $47 \pm 6$     |
| [SII]                              | $6734.41 \pm 0.06$            | 6730.85                            | $18.0 \pm 3.2$  | $163.4 \pm 5.7$    | $47 \pm 6$     |

**Table 2.** List of observed discrete emission lines from nebulosity around XTE J0111.2-7317. Wavelengths from Allen (1976), Meinel (1965) and Takami et al. (2001).

ton by an excited ion in a metastable state, as one considers progressively higher densities.

In the neighbourhood of the critical densities from  $10^2 - 10^4 \text{ cm}^{-3}$  accurate densities may be derived, but outside of this range the results are indistinguishable from either 0 or  $\infty$  on each side of the critical density. The results in Table 3 (derived from line fits shown in Figure 9) place an upper limit of  $N_e \leq 200 \text{ cm}^{-3}$ .

### 3.3.3 Line velocities.

The heliocentric velocities of the nebular lines are all consistent with a systemic SMC velocity of 166km/s, excepting the [OII]  $\lambda 3726, 3729 \text{\AA}$ . However, these lines lie at the extreme end of the spectral range where the wavelength calibration is less accurate, so this is not believed to represent a real velocity shift.

The FWHM are all consistent with instrumental broadening, with values comparable to those of the calibration arc lines. The resolution of the blue spectrum is such that structure with a velocity dispersion of up to  $\sim 100 \text{ km/s}$  could lie unresolved, whereas the red spectrum limits such structure to  $\sim 30 \text{ km/s}$ . This result argues strongly against a SNR hypothesis for the nebulosity; even 'old' SNR display expansion velocity dispersions of several hundred km/s (Lozinskaia, 1980).

### 3.3.4 Spatial distribution of nebular lines.

The full known extent of the nebulosity is defined by the narrowband H $\alpha$  image seen in Figure 8. Whether this represents the true distribution of material in the structure or is more a reflection of the state of ionization can best be inferred by looking at the distribution of emission from different atoms and ionization states.

Representative cross-sections along the spatial axis of the spectral images are shown in Figure 10, taken through the mid-point of the detected emission lines with an appropriate width of pixels sampled (mostly 3) depending upon the FWHM. These plots thus show the spatial distribution of emission from each emission line; with the caveat that the

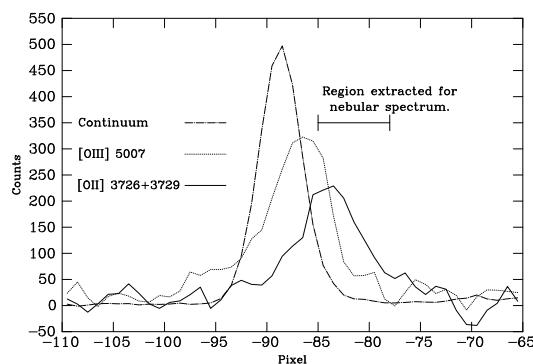


**Figure 10.** Cross sections through the full widths of the [OII] and [OIII] emission lines. The stellar contribution has been subtracted, and is shown for reference. Profiles have been Gaussian smoothed with  $\sigma = 0.7$ .

Be star produces a peak at its spatial location. This arises from both photospheric emission and from the circumstellar disc. These peaks were removed by subtracting an extracted profile derived by interpolation of the continua adjacent to each spectral line, in a manner analogous to sky subtraction in conventional spectral reduction. This was relatively successful for those lines which have no photospheric or circumstellar counterpart: [SII], [O II] and [OIII], though [O II] was affected by the rapid non-linearly declining response of the CCD at short wavelengths.

In the case of the Balmer lines the combined spatial profile from the photosphere and circumstellar disc has the same FWHM in the spatial direction as the continuum, but must be scaled to account for the circumstellar emission.

The orientation of the slit for the ESO blue spectrum - [OIII], [OII], H $\beta$  and H $\gamma$  data is NW - SE through the star and the brightest part of the nebulosity, thus in the context of the bowshock scenario it is usefully aligned along the direction of the standoff distance  $l$ . The [OIII] line was expected as it is observed to be amongst the strongest lines in many nebulae, including other bowshock nebulae, HII regions and PNe.

Narrow band imaging of the field has not produced a detection at [OIII]  $\lambda$ 4959,5007 and in the spectral data it is detected only weakly from the nebular regions brightest in  $H\beta$ . It is however observed as a strong feature from regions much closer to the star itself, to the extent that extraction of the stellar spectrum shows strong features at the aforementioned wavelengths (Figure 2), whereas extraction of the neighbouring nebular spectrum detects them only very weakly. This can be understood with reference to Figure 10 which shows spatial profiles of the [OII] and [OIII] emission lines along the spatial axis.

Whilst the [OIII] emission peaks close to the stellar location and rapidly drops off,  $H\beta$  is observed to considerably larger distances. The [OIII] emission profile is much more symmetric around the Be star, with only minor enhancement in the direction of strongest Balmer emission. Additionally [OIII] is seen from the NW side of the Be star where there is negligible Balmer emission. Where  $H\beta$  and  $H\gamma$  are brightest there is scarcely any [OIII] emission at all.

The  $H\beta$ ,  $H\gamma$  and [OII] emission appear to be coincident, though few conclusions can be drawn from the weak  $H\gamma$  detection. All are seen only to the SE side of the Be star, in a manner totally consistent with the distribution seen from the  $H\alpha$  image in Figure 8. Detection from pixels 75.5 to 92.5 implies an angular diameter of  $13.9''$ , or 4.3 pc.

The SAAO red spectrum -  $H\alpha$  and [SII] - shows the distribution of nebular  $H\alpha$  emission. The size of the nebulosity appears to be the same as that of  $H\beta$  and  $H\gamma$ , with detection out to slightly larger radii because of the much stronger signal. [SII] appears to trace the  $H\alpha$  exactly.

### 3.4 Nebular classification.

If a spectral classification of B0.5-B1 (CHR and Covino et al, 2001) is accepted it becomes possible to calculate the Strömngren radius within which a uniform cloud of H is completely photoionized (note this does not apply to the hollow bowshock model) and would be expected to emit  $H\alpha$ . This radius is sensitive to spectral class around B0, in that this classification sensitively determines the Lyman continuum flux  $Q_0$  depending upon the details of the stellar model used. Vacca et al. (1996) tabulate  $Q_0$  for O3-B0.5V stars, so though one must perform an extrapolation to yield a result for B1, the function is a smooth one and so the result expected to be accurate. Incorporating the Martins et al. (2002) downward revision by 40% of Vacca et al.'s  $Q_0$ , one arrives at  $4.8 \times 10^{47}$  at B0.5V and  $2.4 \times 10^{47}$  at B1V.

Suitably modifying the derivation of equation 6A.1.10 from Kitchin (1987), we arrive at the formula

$$R_S = \left( \frac{3Q_0}{4\pi N_e^2 \times 6.5 \times 10^{-15} T_e^{-0.85}} \right)^{\frac{1}{3}} \text{ (metres)} \quad (2)$$

Using the observed nebular radius of 3.05pc requires  $N_e = 7.6 \text{ cm}^{-3}$  at B0.5 or only  $N_e = 5.1 \text{ cm}^{-3}$  at B1V, at the lower end of observed nebular densities, and in agreement with the results of Section 3.3.2 using forbidden line ratios. The use of SMC metallicities, reducing line blanketing effects, raises  $Q_0$  and thus requires slightly higher densities, but this effect is only of the order of a few %.

This suggests the scenario that the nebulosity is simply an HII region, perhaps part of a cloud adjacent to and ion-

|                  |                   |
|------------------|-------------------|
| [OII] 3729:3726  | $1.48 \pm 0.27$   |
| [SII] 6716:6731  | $1.40 \pm 0.31$   |
| [SII]: $H\alpha$ | $0.286 \pm 0.031$ |
| $H\beta$ :[OIII] | $1.69 \pm 0.32$   |

**Table 3.** Diagnostic line ratios from nebulosity around XTE J0111.2-7317.

ized by XTE J0111.2-7317. If so, and considering the fact that the calculated densities are very much at the lower end of the range for HII regions, why is this structure detectable at all? Most OB stars rid their neighbourhood of gas early in their existence via powerful winds. The answer may lie in the fact that as a BeXRB, XTE J0111.2-7317 has a large space motion (van den Heuvel et al, 2000) and has impinged upon a cloud which it has subsequently ionized. If this cloud increases in density towards the south-east (lower left in the images), the slightly smaller radius in this direction can be explained with the Strömngren sphere argument ( $R_S = fn(N_H)$ ), or as an ionization front propogating into the cloud.

#### 3.4.1 The bowshock theory

Stellar bow-shocks form from the ram-pressure interaction of the local interstellar medium with the stellar wind; when the star's velocity exceeds the sound velocity in the ISM material is swept up into a shock front which is detected primarily using one of two techniques: narrowband imaging (mostly  $H\alpha$ ) and IR imaging, mostly using IRAS data. Whereas  $H\alpha$  imaging takes advantage of excited H, the IRAS flux (usually most pronounced in the  $60\mu\text{m}$  band) arises from thermal radiation from swept-up dust originating from the star, heated by shock interactions.

The appearance of a bowshock is clearly heavily dependant upon the angle that the star's velocity vector makes with respect to the plane of the sky. Classic parabolic structures such as Vela X-1 and  $\alpha$  Cam are seen when the star's motion lies almost entirely within this plane. Less clearly defined structures are more commonly seen, though enhanced brightness on one side, such as is observed in XTE J0111.2-7317, is usually apparent (Noriega-Crespo et al, 1997).

Thus the morphology of a bowshock is such that the head or apex of the structure is well defined if viewed side-on, enabling a 'standoff distance'  $l$  to be determined; there is no sharply defined trailing edge. The size of the structure is thus easily characterised only for side-on specimens. In the case of XTE J0111.2-7317, the standoff distance is approximately 3pc, within the range found for other bowshocks tabulated in Table 4.

Comparing the  $60\mu\text{m}$  IRAS image of the  $\alpha$  Cam bowshock in with the XTE J0111.2-7317 nebula reveals an extremely similar appearance. Both nebulae lie within an approximately parabolic perimeter, and though  $\alpha$  Cam itself is not visible in the IRAS image, both stars lie slightly inside the radius of curvature of the nebulosity, agreeing with the theoretical radius of curvature for a stellar wind bowshock of  $(5/3)l$ .

Without doubt a measured space velocity for XTE J0111.2-7317 would be strong evidence one way or the other. The radial velocity has been investigated by cross correlat-

| Object           | Spectral class                      | Standoff dist.(pc) | Space vel.(km/s)      |
|------------------|-------------------------------------|--------------------|-----------------------|
| XTE J0111.2-7317 | <i>B0Ve</i> <sup>1</sup>            | 3.0                |                       |
| Vela X-1         | <i>B0.5Ibe</i> <sup>2</sup>         | 0.48               | ~ 50km/s <sup>8</sup> |
| $\alpha$ Cam     | <i>O9.5Iae</i> <sup>3</sup>         | 5.1 <sup>6</sup>   | 48 <sup>7</sup>       |
| 0623+71          | <i>CataclysmicVar.</i> <sup>4</sup> | 0.08               | ~ 100km/s             |
| Betelgeuse       | <i>M2Iab</i> <sup>5</sup>           | 0.8                | 56                    |

**Table 4.** Sizes of some stellar bowshocks and spectral classification of their associated stars. Sources 1:This work, 2:Kaper et al. (1997), 3:Noriega-Crespo et al. (1997), 4:Hollis et al. (1992), 5:Noriega-Crespo et al. (1997), 6:van Buren and McCray (1988), 7:Stone (1979), 8:Comeron & Kaper (1998)

ing the blue ESO spectrum with that of a velocity standard, but errors of 50km/s and a result consistent with zero were sufficiently large to preclude any conclusions being drawn, probably because of the low S/N of the spectrum. Studies of specific lines would seem to suggest a limit on  $v_r$  of less than 10km/s. The bowshock appears however to be nearly edge on, in which case most of the stellar velocity is oriented in the plane of the sky and a modest or zero  $v_r$  would be expected.

Comeron & Kaper (1998) have performed numerical simulations of bowshocks in a number of cases. One of their findings is that in low velocity cases ( $v_* \ll 100\text{km/s}$ ), of which XTE J0111.2-7317 is an example as a BeXRB, the bowshock becomes much thicker as the assumption of instantaneous cooling, implicit in the above equation, fails. The resulting thick layer of hot gas, bounded on one side by the stellar wind, and on the other by the ISM, certainly can explain the broader appearance of XTE J0111.2-7317's nebula compared to that of Vela X-1.

A second consequence is that peak density occurs at  $1.5 - 2l$ , somewhat away than the balance point  $l$  predicted by simple momentum balance. Rearranging equation 16 of Raga et al. (1997) to incorporate metallicity dependences (Vink et al, 2001) of  $\dot{M}$  and  $v_w$  gives the following equation balancing the ram pressure of the ISM with that of the expanding stellar wind at the standoff point, a distance  $l$  from the star.

$$N_{ISM} = \frac{\dot{M}_{Z=1} Z^{0.82} v_w}{4\pi l^2 m_H v_*^2} \quad (3)$$

Using a solar metallicity mass loss rate of  $3 \times 10^{-8} M_{\odot} \text{yr}^{-1}$  (Vink et al, 2000), a wind velocity of 1000km/s, the assumption of a pure hydrogen ISM, system velocity  $V_w = 15\text{km/s}$  (mean BeXRB velocity), and  $l = 3.0\text{pc}/(1.5 - 2)$  requires an ISM density of  $0.02 - 0.034\text{cm}^{-3}$ . This value is low for any ISM, particularly in a gas rich galaxy like the SMC where densities of less than  $0.1\text{cm}^{-3}$  are uncommon. The assumption of an unusually high wind speed and/or mass loss rate can reconcile this situation, but both seem somewhat unlikely.

Though this is clearly some way from an exact method of calculating the ISM density, it seems safe to conclude that it must be low if we believe the bowshock interpretation. We are therefore led to questioning why this is the only one known around a BeXRB. The requirement of supersonic velocity may be the reason; the typical ISM sound speed of  $v_S \alpha N^{1/2} \sim 10\text{km/s}$  is only slightly below the mean BeXRB velocity of 15km/s (van den Heuvel et al, 2000), so perversely it could be only the BeXRB systems travelling

through relatively tenuous regions that are capable of producing bowshocks.

The argument in Section 3.4 concerning the Strömgren radius around the B star does not apply to such thin shells. Equation 21 of Comeron and Kaper (1998) considers the flow of material into the bowshock to find the required ionizing flux - using the values given above, the flux necessary to fully ionize the material in the shock front is only  $4 \times 10^{42} \text{sec}^{-1}$ , which is several orders of magnitude less than a B0.5-B1 star provides. Thus we expect to see  $H\alpha$  emission from the bowshock.

Whilst the [SII]: $H\alpha$  ratio of 0.286 is below the threshold of 0.4 usually accepted as clear evidence of shock excitation, it is significantly above the typical values for photoionized nebulae which mostly lie below 0.2. This suggests the possibility that a combination of photoionization and shock excitation may be at work.

### 3.4.2 Comparison with other bowshock spectra

The discovery and study of bow-shocks around high velocity stars is a relatively new facet of astronomy. Few published spectra exist - spectra of only two other stellar wind bowshocks have been found in the literature: Vela X-1 (Kaper et al, 1997) and a CV system 0623+71 (Hollis et al, 1992). Both sources show strong Balmer emission as well as [OIII] and [SII] lines, in common with XTE J0111.2-7317. Additionally the 0623+71 spectra show strong [OII] lines much like XTE J0111.2-7317. The only significant difference is the absence of [NII] lines in the XTE J0111.2-7317 spectra, though the Vela X-1 spectra show them so weakly that if present in XTE J0111.2-7317 at a similar level they would not have been detected. Thus the Vela X-1 nebular spectrum is not significantly different to that of XTE J0111.2-7317, strengthening the bowshock hypothesis.

Essentially the XTE J0111.2-7317 nebular spectra are qualitatively similar to both of the bowshock spectra shown, in particular that of Vela X-1. This is to be expected as the XTE J0111.2-7317 system far more closely resembles Vela X-1 than 0623+71.

The presence of [OIII] far from the presumed shock interaction suggests photoionization as the mechanism for its excitation rather than shock processes; Noriega-Crespo and Garnavich (1992), in their studies of bowshocks of Herbig-Haro objects, confirm earlier findings (Dopita et al, 1984) that shock velocities of 80km/s are required to provide sufficient excitation to produce [OIII]  $\lambda 4959, 5007$ , and spectra do not reveal such velocities to be present. Bowshock theory also does not predict this order of velocity.

### 3.4.3 The HII region hypothesis.

A high [OIII]: $H\beta$  ratio is a diagnostic of photoionization from the Be star's UV flux, comparable to the strong [OIII] lines seen in planetary nebulae caused by the white dwarf's UV flux. The observed ratio (Table 3) is somewhat higher than seen in the two available bowshock spectra and is typical of HII nebulae and at the large end of the distribution for SNR (Fesen et al, 1985; Blair & Long, 1997).

The observation of a small [OIII] nebula coincident with the central star raises a possible problem for the bowshock theory. If this material truly lies within the larger  $H\alpha$  nebula, it would appear to argue against the bowshock theory, as the interior of its paraboloidal shell is considered to be empty, excepting the expanding rarified stellar wind. The simulation work of Comeron & Kaper (1998) allows for some material to pervade this region, but probably not as close to the star as we observe. Therefore in this scenario the [OIII] emission must lie on the surface of this shell. In the case of XTE J0111.2-7317 however, the chances of one patch of emission lying so well centred on our line of sight to the star seem remote - the best explanation for this must be that the [OIII] emission arises physically within the bounds of the  $H\alpha$  nebula, particularly as a Strömngren sphere argument can account for the relative sizes and locations of these features in this scenario.

Section 3.3.4 shows that the HII, [SII] and [OII] nebulae are approximately coincident. Whereas this flows naturally from a bowshock theory (one is simply measuring the standoff distance  $l$ ), it can also be understood in terms of Strömngren spheres.

In view of the abundance of nebulae within 30' of XTE J0111.2-7317, the association with a gas cloud does not cause any problems. SHASSA (Southern H-Alpha Sky Survey Atlas) (Gaustad et al, 2001) shows large HII regions close by and diffuse emission to be extremely pervasive.

The high space velocity which all BeXRB possess could simply have enabled the star to drift into an interstellar cloud and ionize it; it could not have been in this position long as the surrounding gas would have been blown away by the stellar wind. The mean space velocity of BeXRBs of 15km/s (van den Heuvel et al, 2000) corresponds to 1pc in 11,000 years.

### 3.4.4 SNR hypothesis

Obviously, the presence of the NS in a BeXRB requires there to have been a SN explosion at some stage in the system's evolution. Thus the discovery of a nebula surrounding the system naturally raises the possibility that this may be a SNR, thereby enabling the age of the system in its BeXRB state to be reliably estimated and providing verification of the BeXRB formation mechanism. However, spectral evidence shows that this is not the case.

Even a qualitative comparison of the nebular spectrum reveals that it is much more closely allied both to published bowshock (discussed above) and HII region spectra than to a those of SNR. In addition, several quantitative properties argue powerfully against it being a SNR.

The [SII]: $H\alpha$  ratio is a good distinguishing diagnostic between HII regions and SNRs, and is the standard diagnostic used for classifying nebulae in neighbouring galaxies

where morphology cannot be used (Blair & Long, 1997). With the exception of a handful of extremely low surface brightness HII regions similar to and including the diffuse interstellar gas, the vast majority of such objects have a [SII]: $H\alpha$  ratio of less than 0.4, and usually below 0.2. SNR have values normally significantly in excess of 0.5. Thus with a ratio of 0.286 XTE J0111.2-7317 lies at the upper end of the distribution of HII regions, suggesting the possibility of a shock heating component in addition to photoionization as the dominant mechanism.

The temperature sensitive line ratio [OIII]  $\lambda$ 5007/[OII]  $\lambda$ 3726 +  $\lambda$ 3729 appears to be 0.12 from Table 2, implying a temperature in excess of 70,000K (Figure 7 of Dopita, 1997) this is strongly affected by the photoionized component at small distances from the star; no [OIII] emission is detected from the shock-front itself implying temperatures below those encountered in SNR. Similarly, whilst the [OIII]  $\lambda$ 4363/ $\lambda$ 5007 ratio is traditionally used to provide temperatures in SNR, upper limits to the  $\lambda$ 4363 line ( $3 \times 10^{-17}$  erg/s) combined with the [OIII] line strength can only suggest temperatures below 25-40,000K, in the realm more typical of planetary nebulae than SNR. The negligible presence of  $O^{++}$  at the shock location in itself betrays temperatures of below 40,000K (Dopita 1977). Additionally the lack of [O I]  $\lambda$ 6300,6364 places the system well away from the realm of SNR in the diagnostic diagrams of Fesen et al. (1985).

### 3.5 Other HMXBs

A total of 15 other HMXBs in the Magellanic Clouds were examined for evidence of nebulosity, but none was found. Anything down to a scale of  $\sim 1$  pc and  $H\alpha$  flux density  $\sim 20\%$  of the XTE J0111.2-7317 nebula (which has almost exactly the same  $H\alpha$  surface brightness as the Vela X-1 bowshock) would have been detected. In view of the consistency of the surface brightness of these structures and typical sizes it seems probable that any other similar structures would have been found. Thus the frequency of such objects in our sample is 1 in 15, or 6.7%. This statistic is in exact agreement with the results of Huthoff and Kaper (2001) who searched for IR bowshocks around 15 galactic HMXRBs, and found none except for the well-known case of Vela X-1 (Kaper et al, 1997).

## 4 CONCLUSIONS

The observed characteristics of the nebulosity surrounding XTE J0111.2-7317 have been examined in the context of three possible nebular types: SNR, bowshock and HII region. Of these, the SNR hypothesis is excluded by several line ratios and velocity dispersion. Such properties provide no discrimination between bowshocks and HII regions, but the spatial distribution of line emission from different species matches predictions for an HII region to a high degree, whilst providing only a poor match to the expectations for a bowshock. Overall these results provide good evidence that the nebulosity surrounding XTE J0111.2-7317 is a conventional HII region.

The x-ray outburst from the 31-s X-ray pulsar in XTE J0111.2 observed with BATSE and RXTE in 1998-1999 exhibited characteristics typical of a giant or type II outburst

in a BeXRB including large spin-up rates,  $Lx \geq 10^{38}$  erg/sq-cm-s, and a correlation between spin-up rate and pulsed flux. However, the temporal profile of the outburst was unusual, consisting of two similar intensity peaks, with the first peak of shorter duration than the second.

Thus, while apparently unusual, XTE J0111.2-7317 appears, in fact, to be a normal SMC BeXRB embedded in a locally enhanced ISM which it has photoionised to create an HII region.

## ACKNOWLEDGMENTS

NJH acknowledges the use of STARLINK software and the support of a PPARC studentship. IN is partially supported by the Spanish Ministerio de Ciencia y Tecnología under grants AYA2002-00814 and ESP2002-04124-C03-03.

## REFERENCES

- Allen, C.W. 1976 "Astrophysical Quantities", pub Athlone.
- Blair, W.P. & Long, K.S., 1997, ApJS, 108, 261.
- Chakrabarty D., Levine A.M., Clark G.W., Takeshima T., Wilson C.A. & Finger M.H., 1998 IAUC 7048.
- Chakrabarty D., Ozaki M., Paul B. & Yokogawa J., 1998 IAUC 7062.
- Chevalier R.A. 1977 ARA&A 15, 175.
- Clark D.H. & Caswell J.L., 1976 MNRAS 174, 267.
- Coe MJ, Haigh NJ & Reig P, 2000, MNRAS 314, 290 (paper CHR).
- Comeron F & Kaper L, 1998, A&A, 338, 273.
- Covino S., Negueruela I., Campana S., Israel G.L., Polcaro V.F., Stella L. & Verrecchia F., 2001, A&A, 374, 1009.
- Dopita M.A., 1977, ApJS, 33, 437.
- Dopita M.A., Binette L., Dodorico S. & Benvenuti P., 1984, ApJ, 276, 653.
- Feast M.W., 1961, MNRAS, 122, 1.
- Fesen R.A., Balir W.P. & Kirshner R.P., 1985, ApJ, 292, 29.
- Finger, M. H. et al. 1999, ApJ, 517, 449
- Fishman, G. J. et al. 1989, in Proc. GRO Science Workshop, ed. W.N. Johnson (Greenbelt: NASA/GSFC), 2
- Gaustad, J.E., McCullough P.R., Rosing W. & van Buren D., 2001, PASP, 113, 1326.
- Hollis J.M., Oliverson, R.J., Wagner R.M. & Feibelman W.A., 1992, ApJ, 393, 217.
- Huthoff, F. and Kaper, L. 2002 A&A 383, 999.
- Israel G., Stella, L., Covino, S., Campana, S. and Mereghetti, S. 1999 IAUC 7101.
- Jahoda, K. et al. 1996, EUV, X-ray, and Gamma-Ray Instrumentation for Astronomy VII, SPIE Proc. 2808, ed. O.H.V. Sigmund & M.Gumm (Bellingham:SPIE), 59
- Kaper L., Van Loon J. Th., Augusteijn T., Goudfrooij P., Patat F., Waters L.B.F.M. & Zijlstra A.A., 1997, ApJ, 475, L37.
- Kitchen C.R., "Stars, nebulae and the interstellar medium", 1987, Published by Hilger.
- Kurucz R.L., 1979, ApJS, 40, 1.
- Levine A.M., Bradt H., Cui W., Jernigan J.G., Morgan E.H., Remillard R., Shirey R.E. & Smith D.A., 1996, ApJ, 469, L33.
- Lozinskaia, T.A., 1980, A&A, 84, 26.
- Martins F., Schaerer D. & Hillier D.J., 2002, A&A, 382, 999.
- Meinel A.B., Avenia, A.F. and Stockton, M.W. 1965, "Catalog of emission lines in astrophysical objects", Optical Sciences Center Technical report, Tucson, Arizona.
- Noriega-Crespo A., van Buren, D. & Dgani R. 1997, AJ, 113, 780.
- Noriega-Crespo A & Garnavich PM, 1992, A&AS, 181, 170.
- Raga, A.C., Noriega-Crespo, A., Canto, J., Steffen, W., van Burren, D., Mellama, G. and Lundqvist, P. 1997 Revista Mexicana de Astronomia y Astrofisica 33, 73.
- Rothschild, R.E. et al. 1998, ApJ, 496, 538
- Saraph H.E. & Seaton M.J. 1970, , 148, 367.
- Stone, R.C. 1979 ApJ 232, 520.
- Takami, M., Bailey, J., Gledhill, T.M., Chrysostomou, A. and Hough, J.H. 2001, MNRAS 323, 177.
- Vacca, W.D., Garmany, C.D. and Shull, J.M. 1996 ApJ 460, 914.
- van Burren, D. and McCray, R. 1988 ApJL 329, L93.
- van den Heuvel E.P.J., Portegies-Zwart S.F.B.D. & Kaper L., 2000, A&A, 364, 563.
- Vink J. S., de Koter A. & Lamers H.J.G.L.M., 2000, A&A, 362, 295.
- Vink J. S., de Koter A. & Lamers H.J.G.L.M., 2001, A&A, 369, 574.
- Wilson, C.A., Finger, M.H., Coe, M.J., Laycock, S., Fabregat, J. 2002, ApJ, 570, 287
- Wilson, C.A., Finger, M.H., Coe, M.J., Negueruela, I. 2003, ApJ, 584 ,996
- Wilson-Hodge, C.A. 1999, PhD Dissertation, University of Alabama in Huntsville